Journal of Geophysical Research: Solid Earth

RESEARCH ARTICLE
10.1029/2018JB016375

Key Points:
- New analysis of wide-angle seismic data from the southern Porcupine Basin
- Evidence for presence of oceanic crust in the southern Porcupine Basin.
- Jurassic rifting propagated from south to north, resulting in nonuniform strain when rifting stopped.

Correspondence to:
T. A. Minshull,
tmin@noc.soton.ac.uk

Citation:
Chen, C., Watremez, L., Prada, M., Minshull, T. A., Edwards, R. A., O'Reilly, B. M., et al. (2018). From continental hyperextension to seafloor spreading: New insights on the Porcupine Basin from wide-angle seismic data. *Journal of Geophysical Research: Solid Earth*, *123*, 8312–8330. https://doi.org/10.1029/2018JB016375

Received 18 JUL 2018
Accepted 12 SEP 2018
Accepted article online 15 SEP 2018
Published online 23 OCT 2018

©2018. American Geophysical Union. All Rights Reserved.

From Continental Hyperextension to Seafloor Spreading: New Insights on the Porcupine Basin From Wide-Angle Seismic Data

C. Chen[1,2], L. Watremez[1,3], M. Prada[4], T. A. Minshull[1], R. A. Edwards[2], B. M. O'Reilly[4], T. J. Reston[5], G. Wagner[6], V. Gaw[6], D. Klaeschen[6], and P. M. Shannon[7]

[1]School of Ocean and Earth Science, University of Southampton, Southampton, UK, [2]National Oceanography Centre, Southampton, UK, [3]Laboratoire d'Océanologie et de Géosciences, University Lille, CNRS, University Littoral Côte d'Opale, UMR 8187, Lille, France, [4]Geophysics Section, Dublin Institute of Advanced Studies, Dublin, Ireland, [5]School of Geography, Earth and Environmental Sciences, University of Birmingham, Birmingham, UK, [6]Geomar Helmholtz Centre for Ocean Research, Kiel, Germany, [7]School of Earth Sciences, University College Dublin, Dublin, Ireland

Abstract The deep structure and sedimentary record of rift basins provide an important insight into understanding the geological processes involved in lithospheric extension. We investigate the crustal structure and large-scale sedimentary architecture of the southern Porcupine Basin, offshore Ireland along three wide-angle seismic profiles, supplemented by 13 selected seismic reflection profiles. The seismic velocity and crustal geometry models obtained by joint refraction and reflection traveltime inversion clearly image the deep structure of the basin. Our results suggest the presence of three distinct crustal domains along the rifting axis: (a) continental crust becoming progressively hyperextended from north to south through the basin, (b) a transitional zone of uncertain nature, and (c) a 7- to 8-km-thick zone of oceanic crust. The latter is overlain by an ~8-km compacted Upper Paleozoic-Mesozoic succession and ~ 2 km of Cenozoic strata. Due to the lack of clear magnetic anomalies and in the absence of well control, the precise age of interpreted oceanic crust is unknown. However, we can determine an age range of Late Jurassic to Late Cretaceous from the regional context. We propose a northward propagating rifting process in the Porcupine Basin, resulting in variations in strain along the rift axis.

1. Introduction

During the rifting of continents, continental lithosphere is stretched until final breakup is reached and an oceanic basin is formed. Magma-poor rifting often results in hyperextension of the continental crust, serpentinization of the mantle beneath the thin embrittled crust (Boillot et al., 1989; O'Reilly et al., 1996; Perez-Gussinye & Reston, 2001), and unroofing of a broad zone of continental mantle (Reston, 2009) before the eventual onset of seafloor spreading. The rift evolution and key geological processes, such as the distribution of strain during rifting and the syn-rift tectonics, are recorded by the crustal structure and the stratigraphic record and thus best determined by a combination of seismic methods (reflection and refraction) and well data.

The Porcupine Basin is one of the largest basins in the Irish offshore (Figure 1) and has a thick Upper Paleozoic to Cenozoic sedimentary infill. The basin currently has a distinct bathymetric expression, reflecting Neogene differential subsidence and under-sedimentation (Praeg et al., 2005; Shannon et al., 2001). Cenozoic subsidence (Tate et al., 1993) increases toward the basin axis and down the axis toward the south, suggesting that crustal thinning might similarly increase and that latitudinal variations in the E-W structure of the basin might reflect different stages of rifting (Reston et al., 2004) from a narrow rift in the north, to a wide, more extended rift and perhaps even a pair of conjugate margins in the south, making it an ideal natural laboratory to investigate rifting processes.

In this paper, we present newly analyzed and interpreted wide-angle seismic data that provide important constraints on the deep structure and the rifting evolution of the southern part of the Porcupine Basin. We use tomographic models of the wide-angle seismic data to define the structure of the crust and upper mantle, while 13 normal incidence reflection profiles provide information on the sedimentary succession and structure.

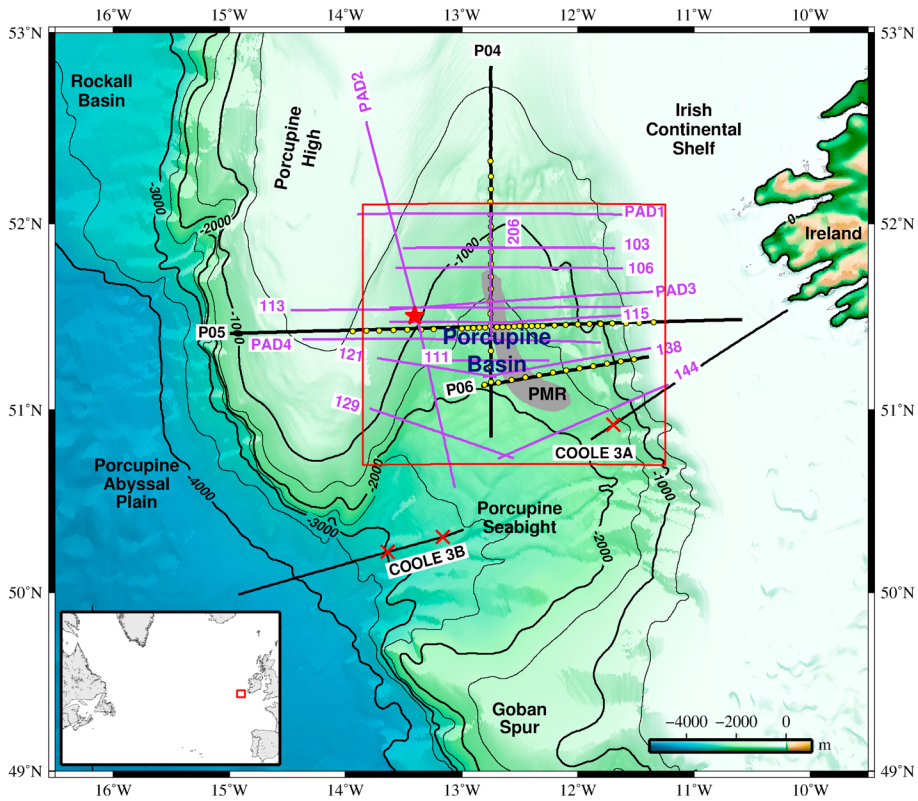

Figure 1. Bathymetric map of offshore Ireland, showing the Porcupine and adjacent basins. Inset shows the location of our study area in North Atlantic. The black lines illustrate the wide-angle shooting profile from M61/2 and COOLE experiment (Makris et al., 1988). Ocean bottom seismometers are illustrated by yellow circles. The red crosses represent the locations of 1-D velocity-depth profiles used in Figure 9. The red rectangle refers to the location of Figures 7 and 10. The purple lines show the seismic reflection profiles used in this research. Porcupine Median Ridge (PMR) is shown in grey (Tate, 1993). Well 43/13-1 is indicated by the red star.

2. Geological Setting

The Porcupine Basin is a V-shaped, deep-water sedimentary basin, located in the North Atlantic southwest of Ireland (Figure 1), between contemporaneous magma-poor continental margins (e.g., Goban Spur; Bullock & Minshull, 2005) in the south, and contemporaneous magma-poor rifts (Rockall Basin) and younger magma-rich continental margins (e.g., Rockall Bank (Joppen & White, 1990); Hatton Bank (Fowler et al., 1989)) in the north. The rifted margins north of the Porcupine Basin are influenced by the North Atlantic igneous province (White et al., 2008). The basin is often considered in several parts: northern and central parts that are both characterized by a N-S trending rift axis, and a southern part, where the rift axis curves toward the SW, before being truncated by Cretaceous oceanic crust of the Porcupine Abyssal Plain (Naylor et al., 2002). For the purposes of distinguishing the changing structure through the Porcupine domain, we consider three regions (northern, central, and southern). Tate (1993) suggested the main rifting of the Porcupine Basin started near the base of the Bajocian, while Bulois et al. (2017) suggested that it started in the Upper Jurassic. Nevertheless, the basin's shape and large-scale structure largely reflect significant lithospheric stretching in Mid-Late Jurassic times, with less pronounced rift episodes in the Permo-Triassic and Early Cretaceous (Shannon, 1991; Tate, 1993).

Based on subsidence analysis of the Porcupine Basin, Tate et al. (1993) estimated that the lithospheric stretching factor increases from less than 1.5 in the north to more than 6 in the south. However, their model lacks constraints from seismic reflection data and well data in the southern Porcupine Basin and does not allow for reduced subsidence resulting from the serpentinization of the uppermost mantle (O'Reilly et al., 1996), to be expected once a stretching factor of ~3 has been reached (Perez-Gussinye & Reston, 2001). Based on the same subsidence data, Tate (1993) proposed that the basin formed by clockwise rotation of the

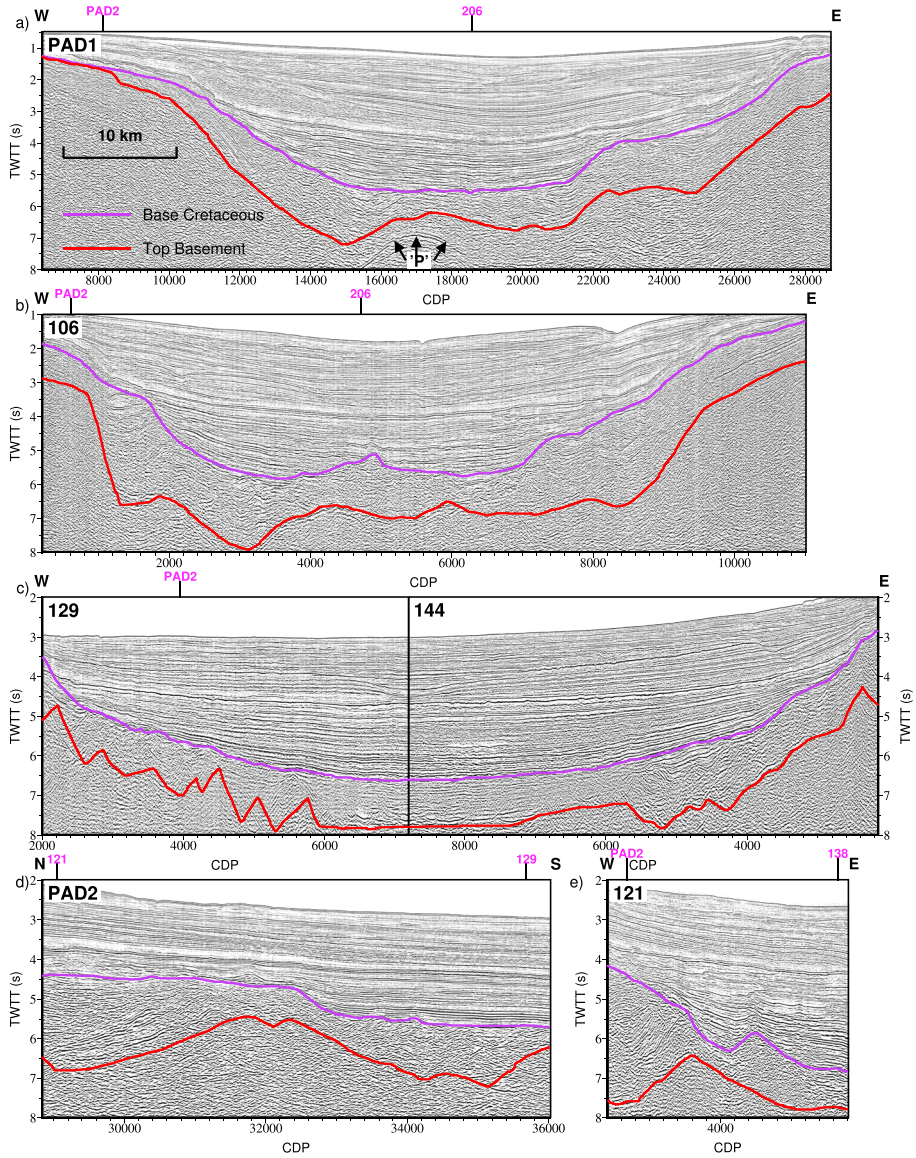

Figure 2. Time-migrated seismic reflection profiles with two major stratigraphic horizons interpreted. The purple horizon corresponds to the Base of Cretaceous. The red line indicates top basement. The intersection points are marked in pink.

Porcupine Bank away from the Irish Mainland and Celtic platforms, leading to a southward increase in stretching factor along the basin axis with a pure-shear stretching mode.

In the northern part of Porcupine Basin, a high-amplitude, bright, and unbroken deep reflector is observed from seismic reflection data, and named the Porcupine Intrabasement Reflection (Johnson et al., 2001) (Reston et al., 2001), subsequently shortened to "P" (Reston et al., 2004) (Figure 2a). Based on seismic reflection data, this feature was formally named the Porcupine Arch (Naylor et al., 2002) and has been interpreted as the top of basement underlying a package of prerift sediments (Johnson et al., 2001) or as a detachment fault separating the crust and serpentinized mantle (Reston et al., 2004). Alternatively, Gagnevin et al. (2017) suggest, on the basis of mapping widespread sill complexes in seismic reflection data, that the Porcupine Arch is the top of a large mafic intrusion that fed these sills. Gravity and wide-angle seismic data have been interpreted to suggest that the Arch is the tectonic expression of mantle serpentinization and the consequent formation of detachment faults (O'Reilly et al., 2006; Readman et al., 2005) and that the rifting of this part of the Porcupine Basin is magma-poor. However, its match to the Moho reflector modeled

from wide-angle seismic profiles in the northern part of the basin (Prada et al., 2017) leads us to favor the feature being the crust–mantle boundary.

An elongate feature in the deep sediments without an evident gravity anomaly, referred to as the Porcupine Median Ridge (PMR; Reston et al., 2004; Tate & Dobson, 1988), is observed where the Porcupine Arch (or *P*) terminates to the south. However, ongoing debate (Calvès et al., 2012) over the structure of the PMR is partly driven by a lack of constraints on the deep structure from available seismic reflection data. The transition between the Porcupine Arch and the PMR coincides with a sharp change in gravity anomaly, attributed to a NW-SE transfer zone that caused a major change in crustal thickness and tectonic regimes across the structure (Readman et al., 1995, 2005; Tate, 1992).

Based on magnetic anomaly data, Lefort and Max (1984) considered the crust in the southern part of the Porcupine Basin to be oceanic in character and suggested limited seafloor spreading in deepest southern basin in mid-Jurassic times (ca. 170 Ma). However, Masson and Miles (1986) reinterpreted the same data set and considered that the amplitudes of the magnetic anomalies (~150 nT peak to peak) are too small to be characteristic of oceanic crust. Based on a seismic refraction study along two ocean bottom seismometer (OBS) profiles (COOLE 3A and 3B, location shown in Figure 1), Makris et al. (1988) suggested that highly stretched continental crust is present in the south of the Porcupine Basin. On the basis of gravity and magnetic modeling along a line between the two COOLE profiles, Conroy and Brock (1989) suggested that the crust is continental in nature and thins rapidly from the eastern continental shelf to less than 8 km in the center of the basin.

3. Data Acquisition and Processing

The seismic reflection data (Figure 1) discussed in this paper are part of three high-quality 2-D surveys acquired by Fugro-Geoteam in 1997 (lines 106, 115, 121, 129, 138, 144, and 206) and Petroleum Affairs Division (Ireland) in 2013 (PAD2) and 2014 (PAD1 and PAD3). Wide-angle seismic data were gathered during F/S Meteor cruise M61/2 in 2004. Here we focus on profiles P04–P06 (Figure 1), The analysis of P05 was presented by Watremez et al. (2016) and the northern part of P04 by Prada et al. (2017); here we analyze data from P06 and the southern part of P04 and integrate results from the three profiles. Both P04 and P06 were acquired with two 32 L Bolt airguns fired at 1-min (~130 m) intervals and OBSs spaced at ~8 km. P04, P05, and P06 are coincident with seismic reflection profiles 206, 115, and 138, respectively (Figure 1).

Along the 220-km-long axial profile P04, 18 OBSs were deployed. Data could be retrieved from 16 of those instruments. Data quality of profile P04 (Figures 3a and 3b) is variable but in general allowed phase identification out to at least 50–60 km. This makes it possible to identify the reflection (PmP) from the crust-mantle boundary (Moho), as well as the head or diving wave within the uppermost mantle (Pn).

Twelve ocean bottom instruments were deployed along the 105-km-long profile P06 (Figure 1). The landward receiver gathers are significantly noisier than those located in the center of the basin, as the water depth decreases sharply when approaching the continental shelf. In general, data from all OBSs allowed phase identification out to at least 40 to 50 km (Figures 3c and 3d), and thus, PmP was identified on most instruments. However, significant delays of the PmP arrival times can be observed compared with those on the northerly instruments (OBS 85 on P04, which is the closest to P05). Pn is not observed on the central instruments because the shooting profile was relatively short.

4. Data Analysis

4.1. Phase Identification and Picking

A drift correction was applied to the OBS clocks, as clock drift can be a source of significant error. The *P* wave arrivals were picked manually on unprocessed seismic records at short offsets and on filtered data for far-offset arrivals. In order to improve the signal-to-noise ratio at far offsets, a minimum phase Butterworth band-pass filter (1-3-16-24 Hz) was applied. Both the hydrophone and vertical geophone were used to identify the best quality arrivals, and then used accordingly for the phase picking. Picking uncertainties were estimated using the signal-to-noise ratio of the traces within ±250 ms of the picked arrivals, using the empirical relationship as in Zelt and Forsyth (1994) and an offset dependent relationship for offsets $<$40 km. The assigned picking uncertainties vary from 20 to 125 ms (Figure 3).

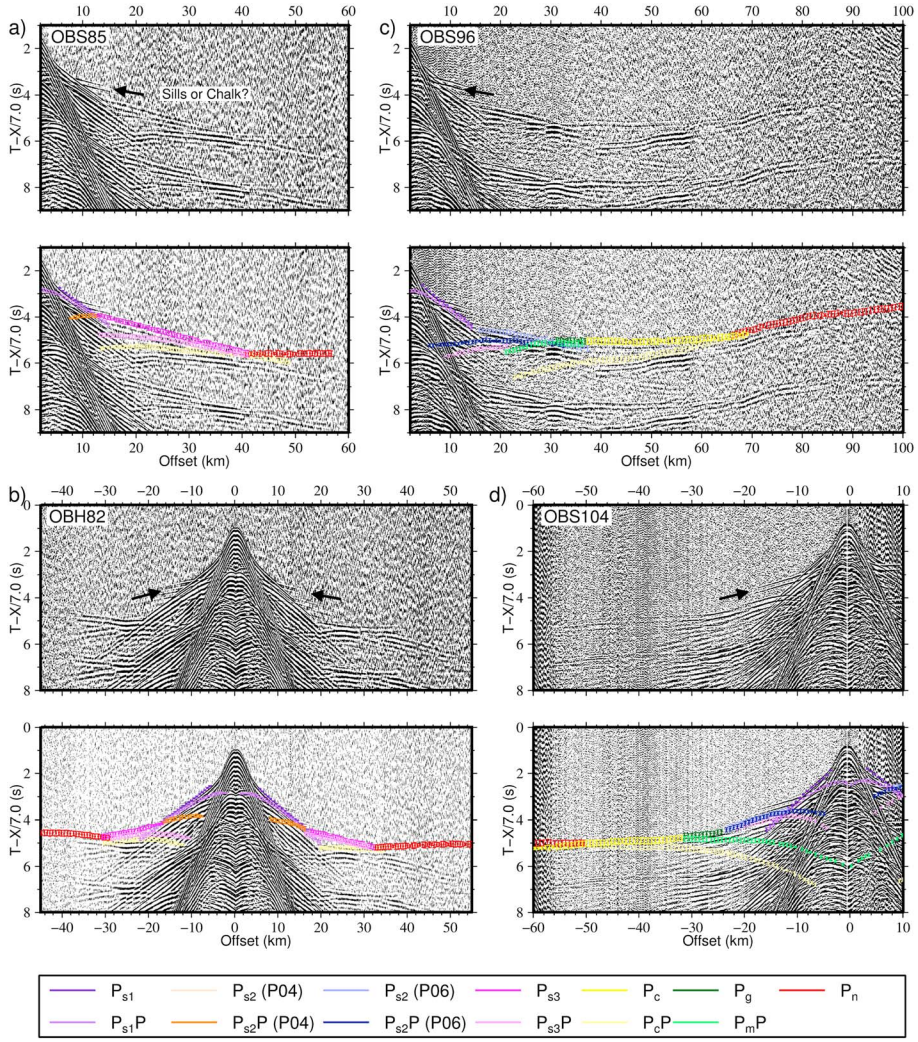

Figure 3. Data and phase picking for instruments 82 and 85 on P04, 96, and 104 on P06. The ocean bottom seismometer (OBS) records are filtered with a 1-3-16-24 Hz band-pass filter for display. The color bars indicating decimated picks (every five) correspond to different seismic phases, as detailed in the bottom legend. The height of each bar represents its uncertainty. The black arrows indicate the high-velocity arrivals from possible sill-complex or chalk.

Along P04, phase identification is difficult due to changes from north to south in the seismic structure of both the sedimentary succession and the basement. In total, two sedimentary phases (Figures 3a and 3b) were identified, with apparent velocities of 1.60–3.5 km/s and 3.75–5.25 km/s. The PmP Moho reflection phase was identified, but no refractions within the crust could be picked.

On profile P06, a sedimentary seismic phase (Figures 3c and 3d) with an apparent velocity 3.15 km/s was identified along the entire line. Beneath this, a higher velocity phase with an apparent velocity 4.6–5.1 km/s was observed on almost all the instruments on the line, also on some of the instruments along P04 and P05. By converting the zero-offset reflection time of this phase into two-way travel time, we infer that it corresponds to the top of the Upper Cretaceous Chalk layer interpreted from the seismic reflection data (Shannon & Bailey, 2007). Upper Cretaceous Chalk has been drilled by well 43/13-1 (Figure 1) underlying basalts on the western flank of the Porcupine Basin (Baxter et al., 2001; King, 2016). This phase is most likely generated either by the Chalk itself or by the Chalk together with an overlaying igneous lava/sill complex. This phase was not used in our tomographic modeling because the associated smoothing deals poorly with velocity inversions. As a shadow zone was created below the high-velocity phase, only one complete pair of refracted and reflected sedimentary phases could be identified, which traveled inside PMR on several western instruments on P06. An additional sedimentary layer below was identified only from reflections on

a few instruments (e.g., OBS96 and 104). The corresponding refractions are difficult to distinguish from those from the basement below, perhaps due to very similar velocities and the reduced thickness of this layer. Two basement layers and the upper mantle were identified with apparent velocities of 5.8–6.3 km/s, 6.6–7.2 km/s, and 7.5–8 km/s, respectively.

4.2. Modeling Strategy

Prior to tomographic analysis, a forward modeling exercise using the code of Zelt and Smith (1992) was carried out to ensure correct phase identification. Picked travel times from profiles P04 and P06 were modeled using TOMO2D (Korenaga et al., 2000), following the approach previously applied to P05 (Watremez et al., 2016). This tomography method uses a hybrid approach based on the graph (Moser, 1991) and ray bending methods (Moser et al., 1992) to calculate the travel time residuals by forward ray-tracing through a given starting model, and then solves a linearized inverse problem using a least squares algorithm (Paige & Saunders, 1982) to reduce the residuals iteratively. In order to retrieve the *P* wave velocity structure and the geometry of reflectors with a high resolution, a joint refraction and reflection travel time inversion was performed following a top-down layer-stripping approach (Sallarès et al., 2011). This approach allows the model to contain sharp discontinuities and avoids building an entirely smooth model. The model was built, layer by layer, resolving the velocity and interface structure of each layer at different steps. For each step, the starting velocity models were defined carefully based on the apparent velocities observed for the given phase, together with the velocities retrieved from the previous layer.

Grid spacing for the models was 0.25 × 0.25 km. The velocity model of profile P04 (Figure 4a) was built in five steps and has six layers. For P06, the model had five layers and one floating reflector for the top of basement, built via six steps. Travel time picks and misfit statistics for the final velocity models of P04 and P06 are detailed in Table 1. Travel time misfits and the chi-square statistics for each individual layer are mostly less than 100 ms and 1.0, respectively.

4.3. Resolution and Uncertainty

4.3.1. Derivative Weight Sum

Ray coverage through the final velocity models of P04 and P06 (Figures 5a and 5e) is represented by the derivative weight sum (DWS), which is a weighted measure of the total ray length through each node in the inversion grid. The models are better resolved where a high DWS is achieved, while low DWS values are associated with regions of poor ray coverage that are not resolved and should not be interpreted. The ray coverage along P04 (Figure 5a) is best between model distances 80 and 180 km, down to 16-km depth. This is the area where ray coverage is the densest and rays are traveling in both directions. Excellent ray coverage was achieved oceanward along P06 (Figure 5e) from model distance 20 to 60 km. Good ray coverage was observed basin-wide up to the Moho depth where we had instrument coverage. Ray coverage was moderate to poor under the continental shelf, where many of the velocity cells are only sampled by unidirectional raypaths.

4.3.2. Monte Carlo Uncertainty Analysis

The Monte Carlo uncertainty test (Korenaga et al., 2000) was used to assess quantitatively the uncertainty associated with the final velocity model. This test evaluates the variability of acceptable solutions for a range of starting models and a range of possible traveltime picks, for a given set of smoothing and inversion parameters (e.g., (Korenaga & Sager, 2012)) and hence is a good measure of relative uncertainty but a poorer measure of absolute uncertainty. For both the profiles, 100 model realizations and tomographic inversions were performed for each layer using the same parameters, which generated the final velocity models in Figure 4, by creating 100 corresponding randomized input velocity models, randomized reflector depths, and randomized traveltime data sets with Gaussian noise. These traveltime data sets were generated by adding randomized timing errors, including a common receiver error (± half the maximum receiver error, ± 62.5 ms), and picking errors.

The parameter ranges used in the starting model for P04 and P06 are listed in Table 2. The average velocity model of P04 (Figure 5b) is very close to the best fitting model (Figure 4a), with sediments thickening toward the north, and similar Moho geometry. The velocity standard deviations (Figure 5c) are generally lower than 0.1 km/s. However, the uncertainties are higher at the southern end of the model because the ray coverage is sparser and unidirectional. In the crust, the uncertainties are slightly higher than 0.1 km/s where no refractions were picked because of a combination of a thin crustal layer and high mantle velocities.

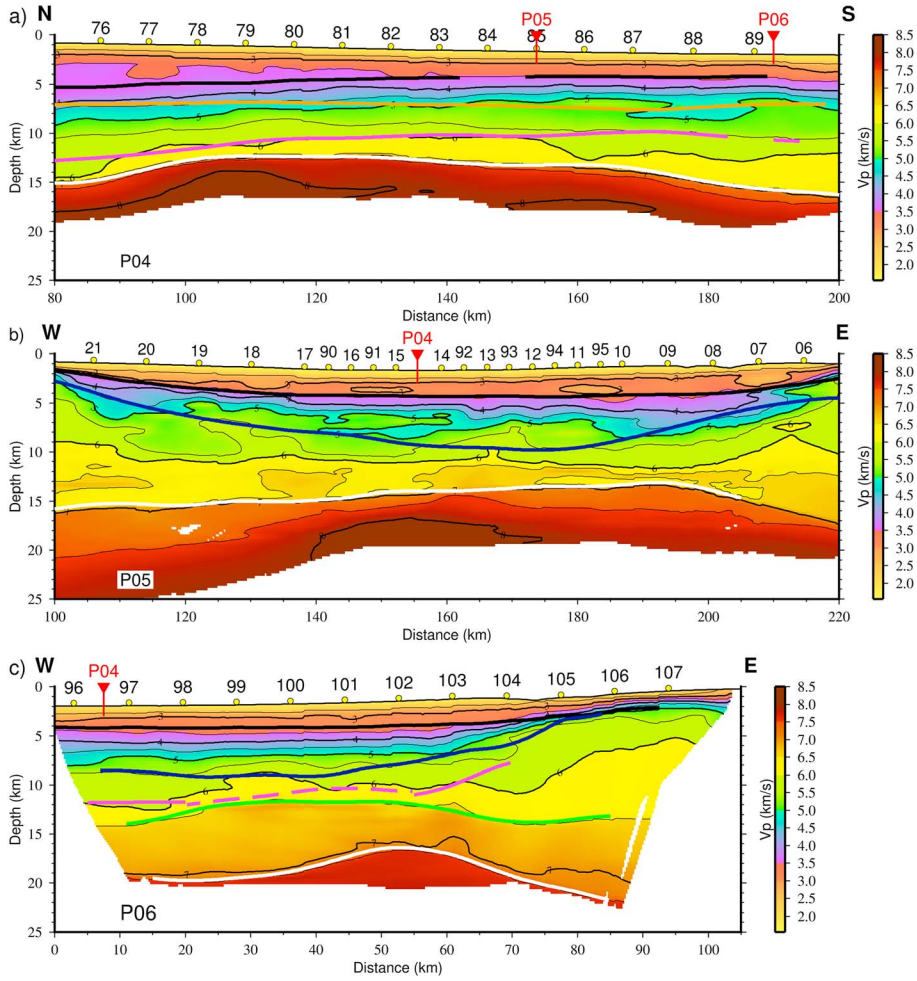

Figure 4. Final velocity models for profile (a) P04, (b) P05, and (c) P06. The colored lines show the interfaces modeled for different layers. The black marks the interpreted base Tertiary; the orange marks the interpreted base Albian; the blue marks the interpreted base Cretaceous; the pink marks the interpreted top of basement (dashed where no reflected phases were observed and modeled). The green illustrates the interface within the crust and white is the Moho. The ted triangles mark the intersection points where the profiles cross each other. Plots have a vertical exaggeration of 1.5.

Table 1
Modeling Statistics for All the Layers Built for P04 and P06

Line	Step	Number of refractions	Number of reflections	t_{RMS} (ms) *refractions*	t_{RMS} (ms) *reflections*	t_{RMS} (ms) *all*	χ^2 refractions	χ^2 reflections	χ^2 all
P04	1	4,634	5,159	14	30	24	0.19	0.41	0.30
P04	2	5,252	2,676	20	52	34	0.19	0.83	0.41
P04	3	8,979	4,658	38	67	50	0.29	0.81	0.47
P04	4	8,979	5,241	33	50	40	0.23	0.39	0.29
P04	5	16,467	5,241	63	49	60	0.45	0.39	0.44
P06	1	2,067	1,978	23.51	31.62	27.77	0.93	0.57	0.75
P06	2	3,452	2,496	45.17	40.06	43.10	1.64	0.57	1.18
P06	3	4,313	3,262	45.32	94.75	70.96	0.46	0.95	0.97
P06	4	6,681	4,527	48.53	76.75	61.51	0.43	0.92	0.63
P06	5	8,121	4,527	51.90	77.32	62.21	0.50	0.89	0.64
P06	6^{Ref}	8,121	874	115.44	125.63	116.44	2.85	6.29	3.18

Note. t_{RMS} is root-mean-squared traveltime residual; χ^2 is normalized chi-square. 6^{Ref} represents the step to invert the separate floating reflector (pink interface in Figure 4c) with all the refractions together.

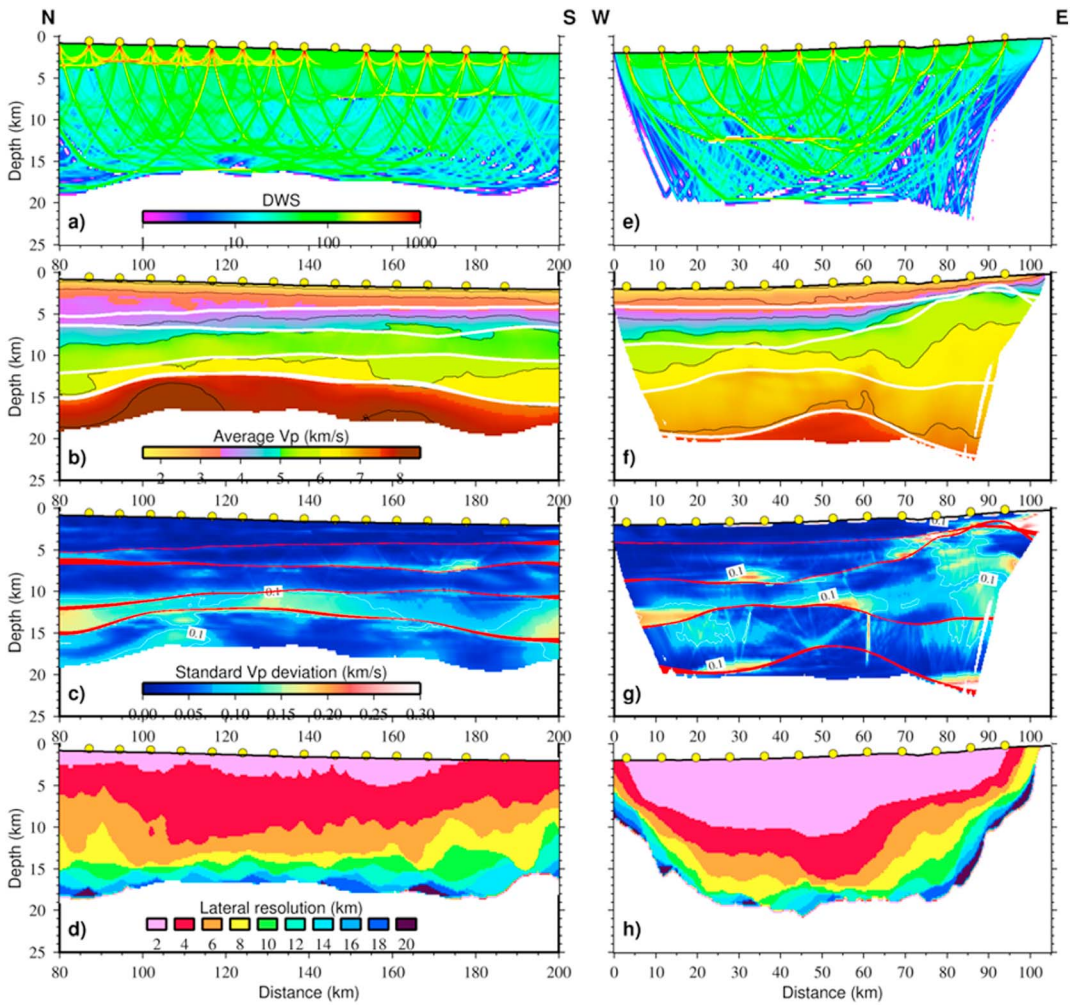

Figure 5. Derivative weight sum of seismic rays traced through the velocity model of (a) P04 and (e) P06. Higher derivative weight sum values indicate areas with a higher density of sampled rays. (b and f) The mean P04 and P06 velocity models from the Monte Carlo uncertainty test. The white lines illustrate the average interfaces from all the model realizations for each layer. (c and g) The standard deviations of velocity models derived from all the starting models for each layer, with the thickness of the red lines marking the standard deviations of interface depth. (d and h) The lateral velocity resolution for P04 and P06 from 80 checkboard tests. The colored regions represent the minimum cell sizes can be resolved by the model. The white regions have lateral resolution larger than 20 km or are unsampled. Plots have a vertical exaggeration of 2.0.

Table 2
Ranges of Values Used for the Model Parameterization of P04 in the Monte-Carlo Analysis

Line	Step	V_P top (km/s)	V_P bottom (km/s)	Interface depth (km) North	Interface depth (km) South
P04	1	1.8 ± 0.05	4.0 ± 0.2	5 ± 0.5	4 ± 0.5
P04	2	3.5 ± 0.2	5.0 ± 0.3	7.5 ± 1	7.5 ± 1
P04	3	4.8 ± 0.2	6.0 ± 0.5	10 ± 2	10 ± 2
P04	4	6.0 ± 0.4	7.0 ± 0.3	25 ± 5	20 ± 5
P04	5	7.5 ± 0.4	8.0 ± 0.1	28.5 ± 2.5	28.5 ± 2.5
P06	1	2.5 ± 0.125	3.0 ± 0.15	5 ± 1	
P06	2	3.5 ± 0.175	5.5 ± 0.275	10 ± 1	
P06	3	5.7 ± 0.285	6.2 ± 0.31	14 ± 2	
P06	4	6.7 ± 0.67	7.1 ± 0.71	18 ± 2	
P06	5	7.5 ± 0.75	8.1 ± 0.81	18 ± 2	

Along P06, the average velocity model (Figure 5f) of P06 is very close to the best fitting model (Figure 4c). The crust beneath the continental shelf exhibits velocity uncertainties of ~ ± 0.1 km/s from 75 to 90 km, which are related to insufficient ray coverage. At 25–35 km of profile distance, the higher velocity zone observed from depth 7 to 9 km on the model (Figure 4c), which corresponds to the location of the PMR shows uncertainty of approximately ± 0.1 km/s. Two lobes of high uncertainties ~ ± 0.1 km/s appear in the upper layer of crust due to the sharp geometry adapted from the upper reflector in the starting model.

4.3.3. Resolution Test

We performed a series of checkboard tests of model resolution to estimate the lateral resolvability of the models (Zelt, 1998). This allowed us to estimate the smallest feature that can be resolved for each model cell. For

both profiles, we perturbed the final tomographic model with a cell of 5% positive and negative velocity anomalies and traced and calculated synthetic arrival times corresponding to our picks. These travel times were then perturbed with random noise as in the Monte Carlo test and inverted together with the final model. For each square cell size (increasing every 2 km from 2 to 20 km), we tested in total of eight checkboard patterns, including opposite polarity for the cell, 45°rotation of the cell, and cells shifted by half of the cell size vertically and horizontally to remove the effects of polarity and registration.

The semblance (resolvability) was then calculated between the input and output patterns within a 5-km operator radius. The checkerboard pattern is considered to be well resolved if the semblance ≥0.7 (Zelt, 1998). The semblance grids for each cell size are then averaged and interpolated to show the minimum cell size can be resolved at each velocity node.

A good resolution of 4 km along P04 is obtained between model distances 100 and 170 km, down to 8-km depth (Figure 5d). Thus, the structure sizes that can be resolved then increase gradually with depth. A structure size of at least 2 km (smallest perturbation pattern) is resolved in the central basin along P06, down to 10-km depth (Figure 5h). Slightly larger structures with a size of 4 km can be resolved at 13-km depth on the basin flank and up to 17-km depth from 40 to 60 km along the model. Generally, the resolution within the basement allows us to interpret structures on a length scale of 6 km and for the lower basement layer, 8 km.

4.4. Seismic Reflection Data

In order to gain further constraints on the crustal structure and the tectono-sedimentary evolution of the basin, the distribution of sediments and two-way travel time (TWTT) to top of basement were mapped on time-migrated seismic reflection data by tracing the stratigraphy away from well 43/13-1 (Figure 1), and also taking into account previous interpretations of individual or multiple profiles (Baxter et al., 2001; Calvès et al., 2012; Johnson et al., 2001; McDonnell & Shannon, 2001; Moore & Shannon, 1995; Naylor et al., 2002; Reston et al., 2004).

Seismic reflection data used in this study are generally of very good quality and reveal a wealth of seismic stratigraphic information (Figures 2 and 6), especially in the Cenozoic to Cretaceous successions (Shannon & Bailey, 2007). The Base Cretaceous unconformity that we picked is characterized by a well-defined strong reflective event that appears to separate the interpreted postrift and synrift sections and deepens from the continental shelf to the central basin. However, these data generally fail to clearly image the top of basement and the Moho, so could not be used to constrain these boundaries in our velocity models. In addition, the lack of deep borehole information in the basin makes it difficult to identify a precise reflector corresponding to the top of the basement. We picked a horizon that maps the bottom of titled fault blocks, above which the sediments exhibit clearly layered features. We are confident that basement rocks are not present above this horizon but cannot exclude the possibility that poorly imaged sediments are present beneath it.

We have compared these horizons with the reflectors modeled from the OBS data (Figure 6). The Base Cretaceous interface (blue line in Figures 6d and 6f) inferred from wide-angle data corresponds in general to the Base Cretaceous horizons (purple lines in Figures 6c–6f) picked on the reflection data. The variation of the Base Cretaceous unconformity along P04 makes the OBS modeling of this interface quite difficult, so a more consistent horizon above the Base Cretaceous was modeled (orange reflector in Figure 4a), which corresponds to the Base Albian horizon. Beneath the Base Cretaceous unconformity, pre-Cretaceous sediments with a maximum velocity of 5.8 km/s were observed at the southern end of P04 and both sides of the PMR on P06. A perfect match was not achieved between horizons inferred from wide-angle and normal incidence data because the OBS data become more complex with increasing depth and normal incidence reflections become more difficult to pick.

On 13 seismic reflection profiles, we interpret a postrift sedimentary unconformity (Base Cretaceous) and the top basement (Figures 2 and 6). These two horizons were then interpolated into isochron maps (Figure 7).

5. Results

5.1. Velocity Models

The final velocity models show many distinct features including: the geometry of the crystalline basement and the PMR, the thinning of the crust, and the velocities in the upper mantle. The P04 model (Figure 4a)

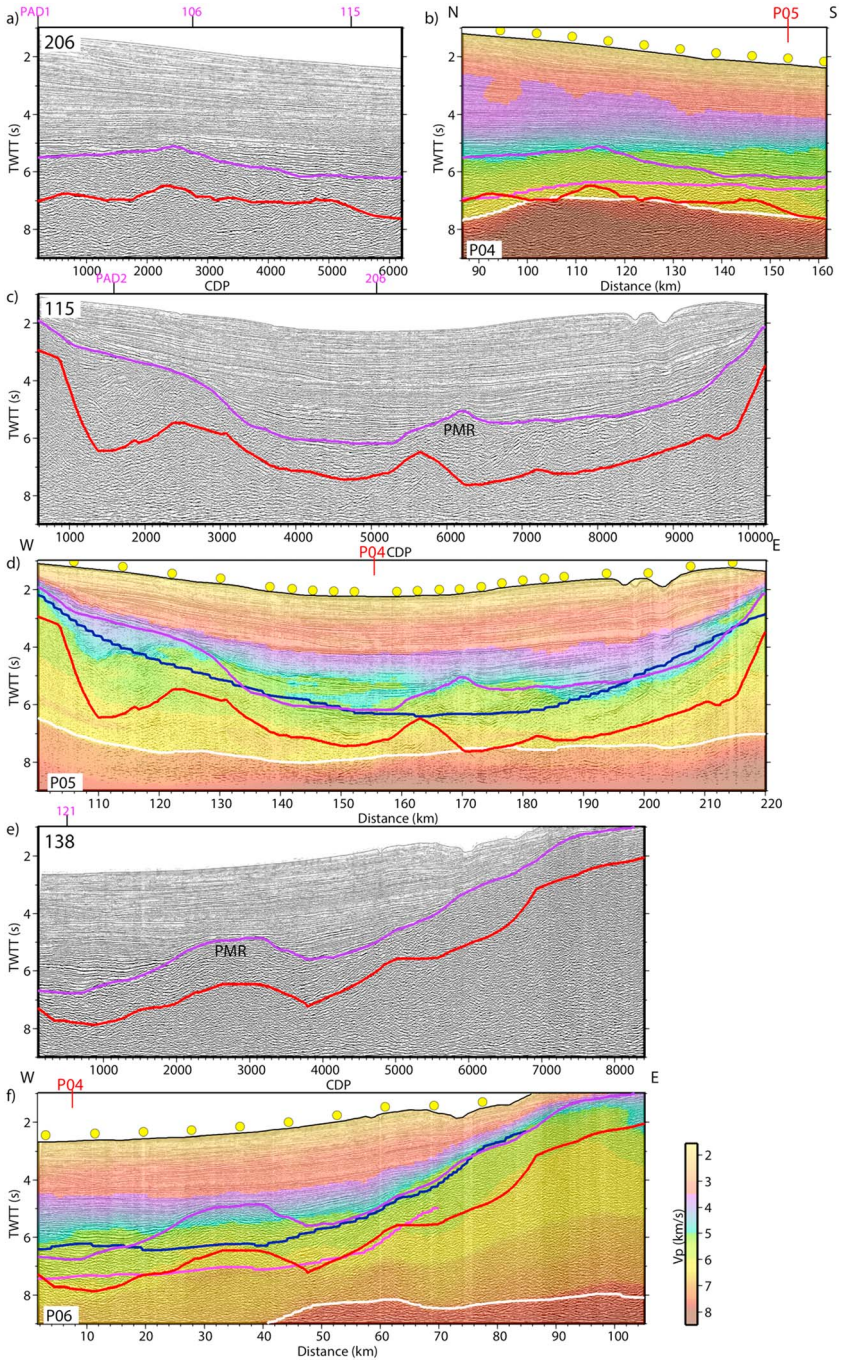

Figure 6. Comparison between velocity models and coincident seismic reflection records. The purple and red lines are the same as in Figure 2. The other colored lines are the same as in Figure 4. (a) Time-migrated seismic reflection record 206. (b) Overlay of the time-converted velocity model P04 on coincident seismic reflection profile 206. (c) Time-migrated seismic reflection record 115, which is coincident with P05. (d) Overlay of the time-converted velocity model P05 on 115. (e) Time-migrated seismic reflection record 138, which is coincident with P06. (f) Overlay of the time-converted velocity model P06 on 138.

shows that the velocity of the sedimentary layers increases southward as the basement deepens, perhaps due to compaction. Lateral variations in the crustal velocities and thickness are also observed along P04. The crust thins from the north and is thinnest at around 100 km. From 100 to 160 km, the crust has a velocity of 6.0–7.5 km/s and a thickness of 2–3.5 km. From 160 to 200 km, Moho depth increases

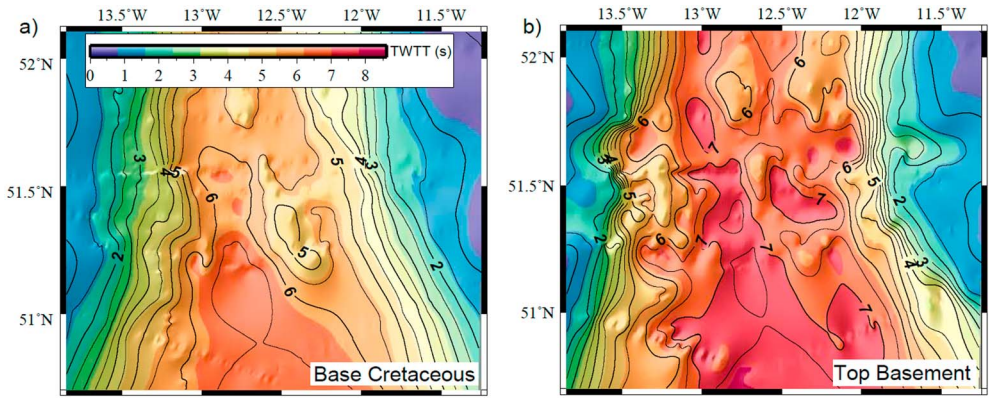

Figure 7. Isochron maps of interpreted stratigraphic horizons. (a) Base Cretaceous unconformity. (b) The top of basement.

significantly from 14 to 18 km. However, the model is less constrained towards its southern end, where there are no more OBS and all the rays are unidirectional.

The P05 model (Figure 4b) shows that velocities beneath the PMR increase rapidly from 5.5 to 7.0 km/s in the center of the basin from 140 to 160 km and increase from 7.5 to 8 km/s within 2 km below the modeled Moho reflector (Watremez et al., 2016). P06 (Figure 4c) shows the velocity structure of the southern Porcupine basin. The uppermost sedimentary layer has velocities of 1.7–3.4 km/s, matching the upper sedimentary layer observed in profile P04 and P05. In the second layer, velocity ranges from 3.5 to 5.5 km/s. The PMR is located at 20 to 40 km within this layer and exhibits slightly higher velocity. The distinctive third interface (pink line in Figure 4c) indicates the presence of a high-velocity sedimentary layer. Velocities in the upper basement layer, interpreted as upper crust, range from 5.8 to 6.5 km/s. Velocities in the lower basement layer, interpreted as lower crust, increase from 6.5 to 7.2 km/s at the Moho, with upper mantle velocities beneath the Moho being ~7.8 km/s. The thickness of the crust varies from ~7 km in the center of the basin (~15 km) to ~8 km at 30 km (beneath the PMR), and ~5.5 km beneath the eastern flank of the basin (~50 km). The crustal velocity (5.0–7.1 km/s) beneath the continental shelf (>75 km) is close to continental velocities observed onshore Ireland (Hauser et al., 2008).

5.2. Seismic Reflection Data

The Base Cretaceous unconformity (Figure 7a) is relatively flat in the basin and deepens steeply in TWTT toward the south as the water depth increases, while the structural high between 51°N and 51.6°N maps the top of PMR. The basin can be divided into distinct zones from north to south based on the reflection characteristics of the upper basement and the lateral coherence of the top basement reflector (Figure 7b). Between reflection profiles PAD1 and 106, where the Porcupine Arch (or P) is imaged (e.g., from 6.8 to 8 s TWTT along CDP 15,400–19,000 in Figure 2a), a series of rift-associated tilted fault-blocks are observed, along with steeply dipping border faults extending into lower crust and connecting with the Porcupine Arch.

For the profiles located in the southern Porcupine Basin where the Porcupine Arch (or P) is absent, the MCS data available for the present paper are not able to image the Moho. From profile 113 to PAD3, the PMR is observed with a prominent high-amplitude seismic event marking its top, and a low-amplitude reflector for the bottom, whereas chaotic reflections dominate the center. In addition, less large-scale faulting and fewer titled fault blocks are observed in the central basin in this area.

A significant change in the basement morphology is observed further south. On profile 138 (Figure 6e), from CDP 2000 to 4000, the basement shows a rough, hummocky surface coincident with the PMR, below which no coherent reflections can be seen. The rough basement morphology terminates at CDP 2000, and a smooth continuous reflector caps the basement to the west before another (possibly volcanic) ridge is seen to disrupt the basement at CDP 5000 on reflection profile 121 (Figure 2e). Furthermore, the central basin lacks identifiable prerift sediments. Further south, a relatively continuous and undisturbed top basement is observed in the middle of basin (Figure 2c), where no prerift sediments were identified.

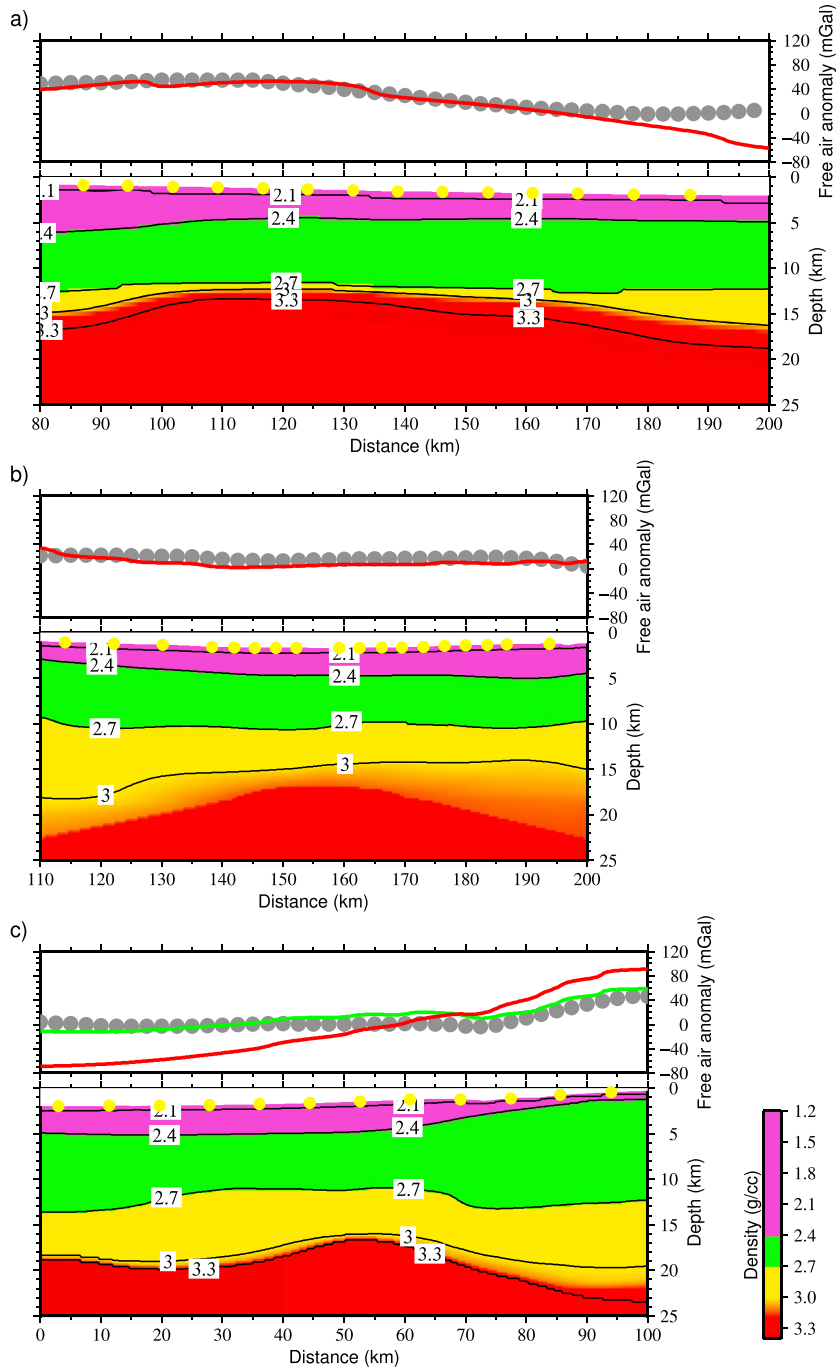

Figure 8. Free air gravity modeling results for (a) P04, (b) P05, and (c) P06. Upper panel: the grey circles mark the observed (free air gravity anomaly). The red line represents the calculated gravity anomaly from the density models below derived from the velocity-density relationships. The green line in (c) represents the calculated gravity anomaly from a model with mantle density variations described in the text. Models were extended 500 km from each edge to avoid edge effects. Lower panel: density model derived from the corresponding seismic velocity model.

5.3. Velocity-Derived Density Models

A comparison between satellite free-air gravity anomaly and the anomaly calculated for density models derived from the velocity structures (Figure 8) can provide further information on the crustal lithology. The final velocity models (Figure 4) were complemented with gravity modeling in different ways. First, the free air gravity anomaly was calculated using the method of Korenaga et al. (2001), by converting the seismic

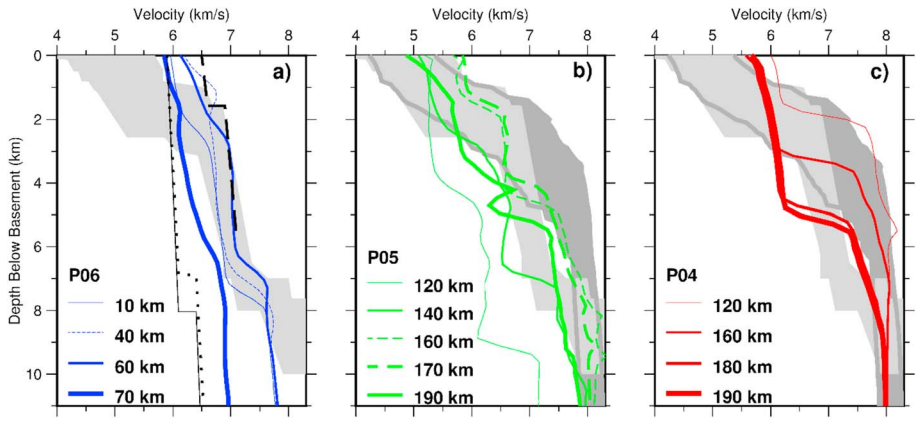

Figure 9. 1-D velocity-depth profiles through the three final velocity models. Depths are measured from the top of the crust in the velocity models (see text). (a) The blue lines represent the 1-D velocity-depth profiles of P06 at different model distances, as shown in the figure. The dashed blue line indicates velocity-depth profiles beneath the PMR. The light grey shading indicates the velocity envelope for Atlantic oceanic crust aged 59–170 Ma (White et al., 1992). The dashed and dotted black line represent the velocity-depth profiles extracted from the western and eastern red cross (Figure 1) of COOLE 3B (Makris et al., 1988), respectively. The thin black line illustrates the velocity-depth profile from COOLE 3A (Makris et al., 1988). (b) The green lines represent the velocity-depth profiles of P05 at different model distances, as shown in the figure. The dashed green lines indicate velocity-depth profiles beneath the PMR. The dark grey shading illustrates the velocity compilation from continent-ocean transition by Minshull (2009). However, as top basement is not modeled by Watremez et al. (2016), the closest reflector (blue line in Figure 4b) is taken to calculate the depth. (c) The red lines represent the velocity-depth profiles of P04 at different model distances, as shown in the figure.

velocities into densities using different empirical velocity-density relationships for different geological layers, to generate a vertically and laterally heterogeneous 2-D density model. For the sediments, Hamilton's (1978) empirical relation for shale was used. For the unaltered mantle (≥8 km/s), density was fixed at 3,300 kg/m^3. Elsewhere, Carlson and Miller's (2003) conversion law for low-temperature serpentinized peridotite was applied (Figures 8a–8c).

The calculated gravity anomaly for P04 (Figure 8a) fits the observed anomaly very well at <160 km. However, an increasing misfit is observed to the south, reaching a maximum 70 mGal. A misfit of the same amplitude occurs on the western side of P06 (Figure 8c), despite the fact that P06 is oblique to the opening direction. The calculated gravity anomaly fits well with the satellite anomaly for P05 (Figure 8b).

The misfits indicate that the adopted velocity-density conversion using a uniform relationship for the whole profile and attribution of all of the gravity anomaly to density variations in the depth range of the velocity models are probably over-simplifications. To address these issues, we added to P06 variations in mantle density that could be attributed, for example, to variability in melt depletion or temperature. Assuming that the average lithospheric thickness is 100 km (Fullea et al., 2014), the lithospheric mantle density at the western end of P06 was set at 3,350 kg/m^3 and decreased gradually to 3,300 kg/m^3 beneath the continental shelf. The fit to the observed data was then improved. The fit for P04 and P06 can be further improved by the insertion of high density blocks (3,000 kg/m^3) at >160 km on P04 and <60 km on P06 to replace the original crustal densities.

6. Discussion

In order to gain insights into the nature of the crust, we compare one-dimensional velocity-depth profiles (Figure 9) through the three velocity models. Interpretations derived from the *P* wave velocity and density models are discussed jointly in this section in addition to features observed on seismic reflection data, gravity data (Figure 10a), and the interpreted top of basement. Three distinct zones (Figure 10b) characterized by different crustal types can be defined in the Porcupine Basin on the basis of their velocities and seismic reflection characteristics.

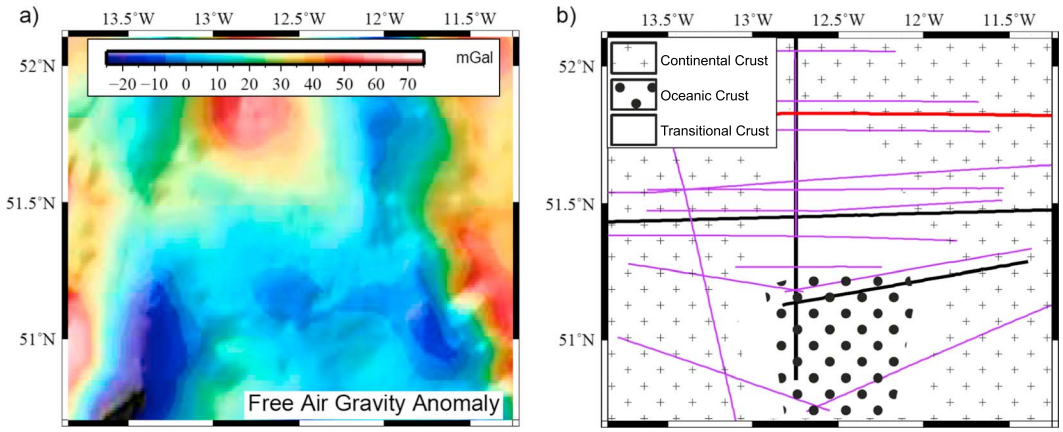

Figure 10. (a) The free air gravity anomaly. (b) Interpreted crustal distribution. The red line marks the location of RAPIDS4, and other lines are as in Figure 1.

6.1. Southern Porcupine Basin

6.1.1. Nature of the Crust

Oceanic crust and highly stretched continental crust are both bounded downward by a sharp jump to ~8 km/s (the Moho) and can have similar thickness and seismic velocities but can be distinguished by their velocity gradients. High-velocity gradients in the top ~ 2 km underlain by low-velocity gradients (~0.1–0.2/s) and a high-velocity down to a Moho at ~6–7 km are typical of oceanic crust (Spudich & Orcutt, 1980); although heavily intruded continental crust may exhibit similar lower crustal velocities, the crust is generally much thicker (Joppen & White, 1990). Where not so intruded, thin, stretched continental lower crust generally has a lower velocity (partly as a result of intense deformation and fracturing) than similar thickness oceanic crust, perhaps with a much lower velocity gradient ($<$0.1/s) (Christensen, 1995). Exhumed mantle in contrast typically has a high velocity gradient (~1/s) representing that downward decreasing amounts of serpentinization until unaltered mantle velocities of ~8 km/s are reached, with a less abrupt Moho (Minshull, 2009). Using these criteria, we can distinguish basement types along the profiles.

The thin high-velocity crust west of 60-km model distance on P06 (Figure 9a) is unlikely to be continental. On both sides of the PMR ($<$20 km, $>$40 km), the upper 2–2.8 km of the basement has an average velocity gradient of 0.27/s and velocities ranging from 5.8 to 6.6 km/s. Beneath this, velocities increase smoothly to 7–7.1 km/s over the next 4–4.5 km, with an ~0.125/s gradient, before increasing sharply to 7.8–8.0 km/s in the uppermost mantle. The velocity-depth profiles at 10 and 60 km (Figure 9a) thus lie mainly within the envelope of normal oceanic crust (White et al., 1992). In between (40-km model distance), the velocity profile represents a slightly thickened version of that at 10 km, consistent with the presence of slightly thickened oceanic crust beneath the PMR. Landward (east) of 60 km model distance (Figure 9a), the crust thickens and is undoubtedly continental at 80 km. The crustal velocities of P05 (Figure 9b) and P04 (Figure 9c) have different trends than those on P06, though the southern part of P04 is poorly constrained.

The crustal velocities observed on P06 are similar to those (Figure 9a) determined in the Porcupine Abyssal Plain on profile COOLE 3B within a thinner oceanic crust, but much higher than those toward the mouth of the Porcupine Seabight, which has a similar crustal thickness (Makris et al., 1988). Based on COOLE 3A and 3B data, the structure in this region comprises an upper crust of 5.9–6.1 km/s and a lower crust of 6.4–6.6 km/s, which were interpreted as continental crust, with an 8 km/s upper mantle. Velocities on P06 are also very close to the oceanic crustal velocities modeled from wide-angle seismic data with a similar strategy in the Gulf of Cadiz, where lithosphere of similar age is inferred (Sallarès et al., 2013). The velocity-depth profiles beneath the PMR show a similar velocity range, but with a thicker layer 3. This slightly thicker layer 3 can be attributed to additional magmatism during the formation of the PMR. The velocity trends here are similar to those of thickened oceanic crust modeled from OBS data in Hatton Bank (Fowler et al., 1989) and Greenland (Hopper et al., 2003). However, the crust in Hatton Bank and Greenland are much thicker, interpreted as resulting from the effects of the Iceland plume.

Many North Atlantic continental margins, for example, Carolina Trough (Tréhu et al., 1989), Hatton Bank (Fowler et al., 1989), and the East Greenland margin (Hopper et al., 2003), have been observed to have lower crustal velocities >7 km/s that are interpreted as underplated or magmatically intruded continental crust. Seaward dipping reflectors have been commonly observed from seismic reflection data at these margins. However, no evidence suggesting the existence of Seaward dipping reflectors has been identified on seismic reflection profiles from the Porcupine Basin. Therefore, our velocity model for P06 is unlikely to represent a volcanic continental margin. Finally, the crust modeled from RAPIDS4 (location in Figure 10b) further north in the Porcupine Basin (O'Reilly et al., 2006) exhibits much lower velocities (6.0–6.5 km/s), providing further support for the suggestion that the crust in the western part of P06 very likely to be oceanic in nature (Figure 10b).

Seismic reflection data (profile 138) show that the central part of the basin has a smooth top basement morphology and a lack of tilted fault blocks and no evidence for prerift sediments (Figure 6e). This morphology provides further evidence for the absence of thinned continental crust at the western part of P06 (< 60 km). An oceanic nature of the crust (Figure 10b) in the southern Porcupine Basin is compatible with the approach we applied for the gravity modeling (Figures 8a and 8c). In addition, the depleted nature of oceanic mantle can result in a greater density than for continental mantle (Jordan, 1988).

6.1.2. Age of the Interpreted Oceanic Crust

Drilling (well 43/13-1) into a synrift sedimentary unit suggests that the postrift sequence may start in the Berriasian, but it cannot provide the exact age of the onset of rifting. Thus, we speculate that the youngest possible age for the oceanic crust is perhaps latest Tithonian, and it cannot be older than Upper Jurassic. During this period, the frequent reversal of a weak magnetic field (Steiner et al., 1998), known as the *Jurassic Quiet Zone* (Larson & Hilde, 1975) would explain the absence of clear linear magnetic anomalies in the Porcupine Basin. Alternatively, the thick Cretaceous sedimentary sequence suggests a high sedimentation rate, and possibly the rapid blanketing by sediments caused sufficiently high temperatures within layer 2 that the basalts lost much of their initial magnetization through low grade metamorphism, as observed in several Mediterranean basins (Vogt et al., 1971) and in Baffin Bay (Keen & Barrett, 1972).

6.2. Northern Porcupine Basin

Crystalline continental crust (5.7–6.5 km/s) was observed at <100 km along P04 (Figure 4a), exhibiting typical continental velocity structure (Christensen, 1995). A southward decrease in crustal thickness and a maximum crustal stretching factor βc >10 at ~120 km suggests that hyperextension of continental crust and even potentially crustal break up toward the south of the Porcupine Basin, as well as mantle serpentinization beneath the Porcupine Arch (Prada et al., 2017). At >100 km along P04, southward thinning of the crust ceases. Furthermore, in seismic reflection data, the top of basement approaches the two-way time of the Moho inferred from wide-angle data (Figure 6b). A clear expression of the Porcupine Arch (or P) disappears, and there is a change in the sedimentary infill (Figure 2b). Thus, we suggest that the southern limit of continental crust occurs at this location (Figure 10b).

Extended continental crust and unambiguous oceanic crust are commonly separated by a zone of transition, generally referred to as the continent-ocean transition (Peron-Pinvidic et al., 2013; Whitmarsh & Miles, 1995). Above the Moho, much of the basement on P05 is characterized by high-velocity gradients underlain by lower gradients, (Figure 9b) and velocity-depth profiles encroach on those of exhumed and serpentinized mantle (Minshull, 2009), particularly toward the rift axis (160–170 km). The velocity structure may suggest the possible presence of partially serpentinized mantle with a downward decrease in the degree of serpentinization. However, these basement velocities would also match well an ~4-km-thick oceanic crust. Moving away from the rift axis (<120 and >190 km), the velocity structure becomes typically continental, and the basement is much thicker.

At >100-km model distance along P04, velocity-depth profiles (Figure 9c) show generally similar velocities to those of exhumed mantle (Minshull, 2009) or thin oceanic crust (White et al., 1992). The RAPIDS4 profile (location in Figure 10b), which crosses P04 at ~110 km, has been modeled with a crustal thickness of around 3 km and velocities ranging from 5.8–6.5 km/s (O'Reilly et al., 2006). This part of the profile has been interpreted as showing thinned continental crust overlaying serpentinized mantle. The difference in velocity between P04 and P05, P06 where they cross is probably due to the major structural changes from north to south along P04. Thus, the TOMO2D inversion finds problems in satisfying all of the data, especially the lateral variations,

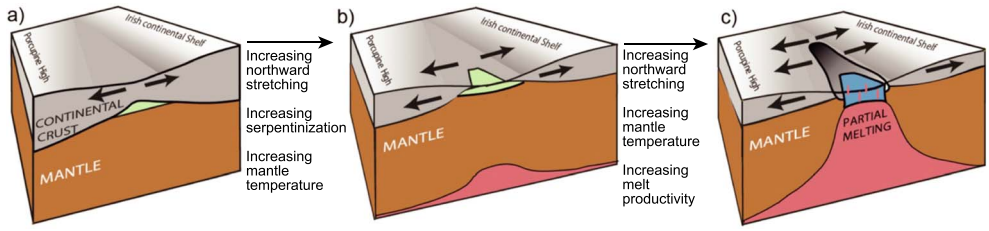

Figure 11. Simplified conceptual model for northward-propagated rifting from magma-poor stretched continental crust to oceanic crust in short distance (adapted from Shillington et al., 2009). The black arrows represent the strain during rifting. The green represents the serpentinization. The blue indicates oceanic crust. Region with gradual change from black to dark grey represents an area of hyper-extended crust with localized mantle exhumation. (a) Main rifting started at Mid-late Jurassic rifting episode. Strain was mainly focused in the south and result in more extension and mantle serpentinization. (b) Along-strike variations in strain leads to northward propagation of rifting and mantle exhumation, as well as a gradual along-strike change in partial melting. (c) Continued rifting and focused magmatic creation in the south leads to incipient seafloor spreading within a narrow region.

resulting in a larger velocity uncertainty than for the other two profiles. Differences can be larger than the standard deviations (e.g., Moho depth shown in Figures 5c and 5g), emphasizing that these plots show relative rather than absolute uncertainties. It is therefore difficult to identify the crustal type confidently in the middle part of P04. However, the deepening of the Moho from 160-km model distance may suggest an increasing thickness of oceanic crust toward the south that is eventually juxtaposed with the oceanic crust observed on P06. Thus, given the oceanic basement characteristics observed on seismic reflection lines 129 and 144, we interpret the crust at the southern end of P04 and on these profiles to be oceanic (Figure 10b). Further south, we only have information from the COOLE lines (Makris et al., 1988), where continental crust was inferred on COOLE 3A and the eastern part of COOLE 3B. These profiles are sparsely sampled (12 OBSs on COOLE 3A, but mainly located on the continental shelf and only 5 OBSs on COOLE 3B) and may-merit reanalysis in the light of our observations. However, if we take their interpretation at face value, oceanic crust may be limited to a small region in the center of the basin.

6.3. Rift Propagation

A set of small basins around Ireland, probably with a NE-SW orientation, started rifting during a Permian to Triassic rifting episode (Naylor & Shannon, 2009; Shannon, 1991). Plate reconstructions suggest that the basin underlying the Porcupine Seabight was narrow at that time and adjacent to the East Orphan Basin (Srivastava & Verhoef, 1992). The main rifting episode, from the Late Jurassic to the Early Cretaceous, progressed diachronously from south to north, leading to the E-W separation of the Grand Banks from central Iberia and then to the SE-NW separation of the southeast margin of Flemish Cap from Galicia Bank (Tucholke et al., 2007). The latter separation was preceded by the opening and subdivision of Orphan Basin (Sibuet et al., 2007). Wide-angle seismic modeling reveals that the East Orphan Basin is underlain by highly stretched continental crust ($<$7-km thickness) extending more than 400 km to Orphan Knoll (Chian et al., 2001; Watremez et al., 2015). A similar crustal structure obtained on COOLE 3B (Makris et al., 1988) may suggest that the basin underlain the Porcupine Seabight also experienced similar rifting around this time. Thus, it is possible that most of the Porcupine Basin continued rifting and grew based on the original geometry, while the southernmost part of the basin went through a similar rifting process to the Orphan Basin. The possible transform fault we observed in the seismic reflection profiles may separate these two regions.

Based on gravity data, Readman et al. (2005) proposed that two transform faults separated the volcanism in the south from the north. In this scenario, a region of narrow segmented sea-floor spreading bounded by NW-SE transform zones may have formed in mid-Late Jurassic-early Cretaceous time. However, our basement map (Figure 7b) does not provide strong support for the presence of transform faults at these proposed locations. Alternatively, we propose that the rifting was driven by nonuniform stretching along the rift axis (Figure 11), with initially more strain focused in the south and therefore more extension there. With the increasing crustal thinning and mantle serpentinization, the mantle eventually becomes exhumed in the south. This difference in strain may have been caused by an earlier rifting in the south. Then the stretching propagated northward, while at the same time the basin continued opening. This simplified conceptual

model explains the structures we observe, composed of hyperextended continental crust in the north, and oceanic crust in the south, without attempting to address the complicated orientation history of the basin. Southward increasing sedimentary thickness and basement patterns support a northward decrease of extension and suggest a corresponding increase in lithospheric thickness during rifting. As a natural consequence of rifting, melt would have been generated by mantle decompression. Melt generation focused in the south as more lithospheric thinning occurred here. With continued stretching and opening, regions of magmatic activity developed into seafloor spreading and oceanic crust was accreted.

Our interpreted rift history has many similarities with that inferred for the Bay of Biscay, which is also a propagating V-shaped ocean basin that opened in the Aptian-Albian time (Jammes et al., 2010). Thus, our analysis sheds further light on the rifting of V-shaped North Atlantic basins (Péron-Pinvidic & Manatschal, 2010).

7. Conclusions

From new wide-angle seismic modeling, we identified three crustal domains in the Porcupine Basin. In the north, continental crust abruptly thins southward to ~5 km thick. Immediately to the south, there is a zone of which basement is uncertain nature. Further south, we suggest the presence of a 7- to 8-km thick unit of oceanic crust, overlain by an ~8-km-thick unit of Mesozoic sediments that are covered by 2 km of Cenozoic sediments. Due to a lack of clear magnetic anomalies and of drilling information, we can only constrain limiting ages for the seafloor spreading to the time of the main rifting episode, that is, Late Jurassic to Early Cretaceous. We propose that the rifting propagated from south to north along the basin axis and was dominated by nonuniform strain. Thus, along-strike variations in crustal and mantle properties are present and stretching eventually led to continental breakup and decompression melting in the southern Porcupine Basin.

Acknowledgments
This research was partially funded by the Irish Shelf Petroleum Studies Group (ISPSG) of Irish Petroleum Infrastructure Programme Group 4. The ISPSG comprises the following: Atlantic Petroleum (Ireland) Ltd, Cairn Energy Plc, Chrysaor E&P Ireland Ltd, Chevron North Sea Limited, ENI Ireland BV, Europa Oil & Gas (Holdings) plc, ExxonMobil E&P Ireland (Offshore) Ltd., Kosmos Energy LLC, Maersk Oil North Sea UK Ltd, Petroleum Affairs Division of the Department of Communications, Climate Action and Environment, Providence Resources plc, Repsol Exploración SA, San Leon Energy Plc, Serica Energy Plc, Shell E&P Ireland Ltd, Sosina Exploration Ltd, Statoil (UK) Ltd, Tullow Oil Plc, and Woodside Energy (Ireland) Pty Ltd. Gravity, magnetic, and seismic data were provided by the Petroleum Affairs Division of the Department of Communications, Climate Action and Environment, Ireland. Seismic reflection data along SPB97 profiles were supplied by Fugro-Geoteam through Conoco-Phillips. PAD and SPBI98 profiles were provided by the Department of Communications, Climate Action and Environment (Ireland). GMT (Wessel & Smith, 1998) was used to prepare all the figures, combined with Seismic-Unix (Stockwell, 1999) for some. T. A. M. was supported by a Wolfson Research Merit award. The wide-angle seismic data used in this study can be accessed via www.pangaea.de.

References

Baxter, K., Buddin, T., Corcoran, D., & Smith, S. (2001). Structural modelling of the south Porcupine Basin, offshore Ireland: Implications for the timing, magnitude and style of crustal extension. *Geological Society, London, Special Publications*, *188*(1), 275–290. https://doi.org/10.1144/GSL.SP.2001.188.01.16

Boillot, G., Feraud, G., Recq, M., & Girardeau, J. (1989). Undercrusting by Serpentinite beneath rifted margins. *Nature*, *341*(6242), 523–525. https://doi.org/10.1038/341523a0

Bullock, A. D., & Minshull, T. A. (2005). From continental extension to seafloor spreading: Crustal structure of the Goban Spur rifted margin, southwest of the UK. *Geophysical Journal International*, *163*(2), 527–546. https://doi.org/10.1111/j.1365-246X.2005.02726.x

Bulois, C., P. Shannon, P. Manuel, C.-R. Nicolas, W. Louise, and D. Jacques (2017). Multiphased extension along continental margins: A case study of the Porcupine Basin, offshore Ireland. *Geophysical Research Abstracts*, *19*, EGU2017-9591.

Calvès, G., Torvela, T., Huuse, M., & Dinkleman, M. G. (2012). New evidence for the origin of the Porcupine Median Volcanic Ridge: Early Cretaceous volcanism in the Porcupine Basin, Atlantic margin of Ireland. *Geochemistry, Geophysics, Geosystems*, *13*, Q06001. https://doi.org/10.1029/2011GC003852

Carlson, R. L., & Miller, D. J. (2003). Mantle wedge water contents estimated from seismic velocities in partially serpentinized peridotites. *Geophysical Research Letters*, *30*(5), 1250. https://doi.org/10.1029/2002GL016600

Chian, D., Reid, I. D., & Jackson, H. R. (2001). Crustal structure beneath Orphan Basin and implications for nonvolcanic continental rifting. *Journal of Geophysical Research*, *106*(B6), 10,923–10,940. https://doi.org/10.1029/2000JB900422

Christensen, N. I. (1995). Seismic velocity structure and composition of the continental crust: A global view. *Journal of Geophysical Research*, *100*(B6), 9761–9788. https://doi.org/10.1029/95JB00259

Conroy, J. J., & Brock, A. (1989). Gravity ad magnetic studies of crustal structure across the Porcupine basin west of Ireland. *Earth and Planetary Science Letters*, *93*, 371–376. https://doi.org/10.1016/0012-821X(89)90036-8

Fowler, S., White, R., Spence, G., & Westbrook, G. (1989). The Hatton Bank continental margin—II. Deep structure from two-ship expanding spread seismic profiles. *Geophysical Journal International*, *96*(2), 295–309. https://doi.org/10.1111/j.1365-246X.1989.tb04452.x

Fullea, J., Muller, M. R., Jones, A. G., & Afonso, J. C. (2014). The lithosphere–asthenosphere system beneath Ireland from integrated geophysical–petrological modeling II: 3D thermal and compositional structure. *Lithos*, *189*, 49–64. https://doi.org/10.1016/j.lithos.2013.09.014

Gagnevin, D., Haughton, P. D. W., Whiting, L., & Saqab, M. M. (2017). Geological and geophysical evidence for a mafic igneous origin of the Porcupine Arch, offshore Ireland. *Journal of the Geological Society*, *175*(2), 210–228.

Hamilton, E. L. (1978). Sound velocity–density relations in sea-floor sediments and rocks. *The Journal of the Acoustical Society of America*, *63*(2), 366–377. https://doi.org/10.1121/1.381747

Hauser, F., O'Reilly, B., Readman, P., Daly, J., & van den Berg, R. (2008). Constraints on crustal structure and composition within a continental suture zone in the Irish Caledonides from shear wave wide-angle reflection data and lower crustal xenoliths. *Geophysical Journal International*, *175*(3), 1254–1272. https://doi.org/10.1111/j.1365-246X.2008.03945.x

Hopper, J. R., Dahl-Jensen, T., Holbrook, W. S., Larsen, H. C., Lizarralde, D., Korenaga, J., et al. (2003). Structure of the SE Greenland margin from seismic reflection and refraction data: Implications for nascent spreading center subsidence and asymmetric crustal accretion during North Atlantic opening. *Journal of Geophysical Research*, *108*(B5), 2269. https://doi.org/10.1029/2002JB001996

Jammes, S., Lavier, L., & Manatschal, G. (2010). Extreme crustal thinning in the Bay of Biscay and the Western Pyrenees: From observations to modeling. *Geochemistry, Geophysics, Geosystems*, *11*, Q10016. https://doi.org/10.1029/2010GC003218

Johnson, H., Ritchie, J., Gatliff, R., Williamson, J., Cavill, J., & Bulat, J. (2001). Aspects of the structure of the Porcupine and Porcupine Seabight basins as revealed from gravity modelling of regional seismic transects. *Geological Society, London, Special Publications*, *188*(1), 265–274. https://doi.org/10.1144/GSL.SP.2001.188.01.15

Joppen, M., & White, R. S. (1990). The structure and subsidence of Rockall Trough from two-ship seismic experiments. *Journal of Geophysical Research*, *95*(B12), 0148–0227. https://doi.org/10.1029/JB095iB12p19821

Jordan, T. H. (1988). Structure and formation of the continental tectosphere, JPet, Special_Volume(1), 11–37.

Keen, C., & Barrett, D. (1972). Seismic refraction studies in Baffin Bay: An example of a developing ocean basin. *Geophysical Journal International*, *30*(3), 253–271. https://doi.org/10.1111/j.1365-246X.1972.tb05812.x

King, C. (2016). A Revised Correlation of Tertiary Rocks in the British Isles and adjacent areas of NW Europe. In C. King, A. S. Gale, & T. L. Barry (Eds.), *East Anglia and London Basin (Paleocene and Eocene)*. *Geological Society of London, Special Report*, 329–375. London: Geological Society.

Korenaga, J., Detrick, R. S., & Kelemen, P. B. (2001). Gravity anomalies and crustal structure at the Southeast Greenland margin. *Journal of Geophysical Research*, *106*(B5), 8853–8870. https://doi.org/10.1029/2000JB900416

Korenaga, J., Holbrook, W. S., Kent, G. M., Kelemen, P. B., Detrick, R. S., Larsen, H. C., et al. (2000). Crustal structure of the Southeast Greenland margin from joint refraction and reflection seismic tomography. *Journal of Geophysical Research*, *105*(B9), 21,591–21,614. https://doi.org/10.1029/2000JB900188

Korenaga, J., & Sager, W. W. (2012). Seismic tomography of Shatsky Rise by adaptive importance sampling. *Journal of Geophysical Research*, *117*, B08102. https://doi.org/10.1029/2012JB009248

Larson, R. L., & Hilde, T. W. (1975). A revised time scale of magnetic reversals for the Early Cretaceous and Late Jurassic. *Journal of Geophysical Research*, *80*(17), 2586–2594. https://doi.org/10.1029/JB080i017p02586

Lefort, J., & Max, M. (1984). Development of the Porcupine Seabight: Use of magnetic data to show the direct relationship between early oceanic and continental structures. *Journal of the Geological Society*, *141*(4), 663–674. https://doi.org/10.1144/gsjgs.141.4.0663

Makris, J., Egloff, R., Jacob, A., Mohr, P., Murphy, T., & Ryan, P. (1988). Continental crust under the southern Porcupine Seabight west of Ireland. *Earth and Planetary Science Letters*, *89*(3-4), 387–397. https://doi.org/10.1016/0012-821X(88)90125-2

Masson, D. G., & Miles, P. (1986). Development and hydrocarbon potential of Mesozoic sedimentary basins around margins of North Atlantic. *AAPG Bulletin*, *70*(6), 721–729.

McDonnell, A., & Shannon, P. (2001). Comparative Tertiary stratigraphic evolution of the Porcupine and Rockall basins. *Geological Society, London, Special Publications*, *188*(1), 323–344. https://doi.org/10.1144/GSL.SP.2001.188.01.19

Minshull, T. A. (2009). Geophysical characterisation of the ocean–continent transition at magma-poor rifted margins. *Comptes Rendus Geoscience*, *341*(5), 382–393. https://doi.org/10.1016/j.crte.2008.09.003

Moore, J., & Shannon, P. (1995). The Cretaceous succession in the Porcupine Basin, offshore Ireland: Facies distribution and hydrocarbon potential. *Geological Society, London, Special Publications*, *93*(1), 345–370. https://doi.org/10.1144/GSL.SP.1995.093.01.28

Moser, T. (1991). Shortest path calculation of seismic rays. *Geophysics*, *56*(1), 59–67. https://doi.org/10.1190/1.1442958

Moser, T. J., Nolet, G., & Snieder, R. (1992). Ray bending revisited. *Bulletin of the Seismological Society of America*, *82*(1), 259–288.

Naylor, D., & Shannon, P. (2009). Geology of offshore Ireland. In C. H. Holland (Ed.), *The geology of Ireland* (pp. 405–460). Edinburgh: Dunedin Academic Press.

Naylor, D., Shannon, P. M., & Murphy, N. (2002). *Porcupine-Goban Region: A standard structural nomenclature system*, Petroleum Affairs Division, Special Publications, 1/02.

O'Reilly, B., Hauser, F., Ravaut, C., Shannon, P., & Readman, P. (2006). Crustal thinning, mantle exhumation and serpentinization in the Porcupine Basin, offshore Ireland: Evidence from wide-angle seismic data. *Journal of the Geological Society*, *163*(5), 775–787. https://doi.org/10.1144/0016-76492005-079

O'Reilly, B. M., Hauser, F., Jacob, A. B., & Shannon, P. M. (1996). The lithosphere below the Rockall Trough: Wide-angle seismic evidence for extensive serpentinisation. *Tectonophysics*, *255*(1-2), 1–23. https://doi.org/10.1016/0040-1951(95)00149-2

Paige, C. C., & Saunders, M. A. (1982). LSQR: An algorithm for sparse linear equations and sparse least squares. *ACM Transactions on Mathematical Software*, *8*(1), 43–71. https://doi.org/10.1145/355984.355989

Perez-Gussinye, M., & Reston, T. J. (2001). Rheological evolution during extension at nonvolcanic rifted margins: Onset of serpentinization and development of detachments leading to continental breakup. *Journal of Geophysical Research*, *106*(B3), 3961–3975. https://doi.org/10.1029/2000JB900325

Péron-Pinvidic, G., & Manatschal, G. (2010). From microcontinents to extensional allochthons: Witnesses of how continents rift and break apart? *Petroleum Geoscience*, *16*(3), 189–197. https://doi.org/10.1144/1354-079309-903

Peron-Pinvidic, G., Manatschal, G., & Osmundsen, P. T. (2013). Structural comparison of archetypal Atlantic rifted margins: A review of observations and concepts. *Marine and Petroleum Geology*, *43*, 21–47. https://doi.org/10.1016/j.marpetgeo.2013.02.002

Prada, M., Watremez, L., Chen, C., O'Reilly, B. M., Minshull, T. A., Reston, T. J., et al. (2017). Crustal strain-dependent serpentinisation in the Porcupine Basin, offshore Ireland. *Earth and Planetary Science Letters*, *474*, 148–159. https://doi.org/10.1016/j.epsl.2017.06.040

Praeg, D., Stoker, M., Shannon, P., Ceramicola, S., Hjelstuen, B., Laberg, J., & Mathiesen, A. (2005). Episodic Cenozoic tectonism and the development of the NW European 'passive'continental margin. *Marine and Petroleum Geology*, *22*(9-10), 1007–1030. https://doi.org/10.1016/j.marpetgeo.2005.03.014

Readman, P., O'Reilly, B., Edwards, J., & Sankey, M. (1995). A gravity map of Ireland and surrounding waters. *Geological Society, London, Special Publications*, *93*(1), 9–16. https://doi.org/10.1144/GSL.SP.1995.093.01.02

Readman, P. W., O'Reilly, B. M., Shannon, P. M., & Naylor, D. (2005). The deep structure of the Porcupine Basin, offshore Ireland, from gravity and magnetic studies. *Geological Society, London, Petroleum Geology Conference Series*, *6*(1), 1047–1056. https://doi.org/10.1144/0061047

Reston, T., Pennell, J., Stubenrauch, A., Walker, I., & Perez-Gussinye, M. (2001). Detachment faulting, mantle serpentinization, and serpentinite-mud volcanism beneath the Porcupine Basin, southwest of Ireland. *Geology*, *29*(7), 587–590. https://doi.org/10.1130/0091-7613(2001)029<0587:DFMSAS>2.0.CO;2

Reston, T. J. (2009). The structure, evolution and symmetry of the magma-poor rifted margins of the north and Central Atlantic: A synthesis. *Tectonophysics*, *468*(1–4), 6–27. https://doi.org/10.1016/j.tecto.2008.09.002

Reston, T. J., Gaw, V., Pennell, J., Klaeschen, D., Stubenrauch, A., & Walker, I. (2004). Extreme crustal thinning in the south Porcupine Basin and the nature of the Porcupine Median High: Implications for the formation of non-volcanic rifted margins. *Journal of the Geological Society of London*, *161*(5), 783–798. https://doi.org/10.1144/0016-764903-036

Sallarès, V., Gailler, A., Gutscher, M.-A., Graindorge, D., Bartolomé, R., Gràcia, E., et al. (2011). Seismic evidence for the presence of Jurassic oceanic crust in the central Gulf of Cadiz (SW Iberian margin). *Earth and Planetary Science Letters*, *311*(1-2), 112–123. https://doi.org/10.1016/j.epsl.2011.09.003

Sallarès, V., Martínez-Loriente, S., Prada, M., Gràcia, E., Ranero, C., Gutscher, M.-A., et al. (2013). Seismic evidence of exhumed mantle rock basement at the Gorringe Bank and the adjacent Horseshoe and Tagus abyssal plains (SW Iberia). *Earth and Planetary Science Letters*, *365*, 120–131. https://doi.org/10.1016/j.epsl.2013.01.021

Shannon, A. M. D., & Bailey, W. (2007). The evolution of the Porcupine and Rockall basins, offshore Ireland: The geological template for carbonate mound development. *International Journal of Earth Sciences*, *96*(1), 21–35. https://doi.org/10.1007/s00531-006-0081-y

Shannon, P. M. (1991). The development of Irish offshore sedimentary basins. *Journal of the Geological Society*, *148*(1), 181–189. https://doi.org/10.1144/gsjgs.148.1.0181

Shannon, P. M., Corcoran, D., & Haughton, P. (2001). The petroleum exploration of Ireland's offshore basins: Introduction. *Geological Society, London, Special Publications*, *188*(1), 1–8. https://doi.org/10.1144/GSL.SP.2001.188.01.01

Shillington, D. J., Scott, C. L., Minshull, T. A., Edwards, R. A., Brown, P. J., & White, N. (2009). Abrupt transition from magma-starved to magma-rich rifting in the eastern Black Sea. *Geology*, *37*(1), 7–10. https://doi.org/10.1130/G25302A.1

Sibuet, J.-C., Srivastava, S., Enachescu, M., & Karner, G. (2007). Early cretaceous motion of Flemish Cap with respect to North America: Implications on the formation of Orphan Basin and SE Flemish Cap–Galicia Bank conjugate margins. *Geological Society, London, Special Publications*, *282*(1), 63–76. https://doi.org/10.1144/SP282.4

Spudich, P., & Orcutt, J. (1980). A new look at the seismic velocity structure of the oceanic crust. *Reviews of Geophysics*, *18*(3), 627–645. https://doi.org/10.1029/RG018i003p00627

Srivastava, S., & Verhoef, J. (1992). Evolution of Mesozoic sedimentary basins around the North Central Atlantic: A preliminary plate kinematic solution. *Geological Society, London, Special Publications*, *62*(1), 397–420. https://doi.org/10.1144/GSL.SP.1992.062.01.30

Steiner, C., Hobson, A., Favre, P., Stampfli, G. M., & Hernandez, J. (1998). Mesozoic sequence of Fuerteventura (Canary Islands): Witness of Early Jurassic sea-floor spreading in the central Atlantic. *Geological Society of America Bulletin*, *110*(10), 1304–1317.

Stockwell, J. W. (1999). The CWP/SU: Seismic Un*x package. *Computers and Geosciences*, *25*, 415–419. https://doi.org/10.1016/S0098-3004(98)00145-9

Tate, M. (1992). The Clare Lineament: A relic transform fault west of Ireland. *Geological Society, London, Special Publications*, *62*(1), 375–384. https://doi.org/10.1144/GSL.SP.1992.062.01.28

Tate, M. (1993). Structural framework and tectono-stratigraphic evolution of the Porcupine Seabight Basin, offshore western Ireland. *Marine and Petroleum Geology*, *10*(2), 95–123. https://doi.org/10.1016/0264-8172(93)90016-L

Tate, M., & Dobson, M. (1988). Syn-and post-rift igneous activity in the Porcupine Seabight Basin and adjacent continental margin W of Ireland. *Geological Society, London, Special Publications*, *39*(1), 309–334. https://doi.org/10.1144/GSL.SP.1988.039.01.28

Tate, M., White, N., & Conroy, J. J. (1993). Lithospheric extension and magmatism in the Porcupine Basin west of Ireland. *Journal of Geophysical Research*, *98*(B8), 13,905–13,923. https://doi.org/10.1029/93JB00890

Tréhu, A. M., Ballard, A., Dorman, L., Gettrust, J., Klitgord, K., & Schreiner, A. (1989). Structure of the lower crust beneath the Carolina Trough, US Atlantic continental margin. *Journal of Geophysical Research*, *94*(B8), 10,585–10,600. https://doi.org/10.1029/JB094iB08p10585

Tucholke, B., Sawyer, D., & Sibuet, J.-C. (2007). Breakup of the Newfoundland–Iberia rift. *Geological Society, London, Special Publications*, *282*(1), 9–46. https://doi.org/10.1144/SP282.2

Vogt, P., Higgs, R., & Johnson, G. (1971). Hypotheses on the origin of the Mediterranean basin: Magnetic data. *Journal of Geophysical Research*, *76*(14), 3207–3228. https://doi.org/10.1029/JB076i014p03207

Watremez, L., Lau, K. W. H., Nedimovic, M. R., & Louden, K. E. (2015). Traveltime tomography of a dense wide-angle profile across Orphan Basin. *Geophysics*, *80*(3), B69–B82. https://doi.org/10.1190/geo2014-0377.1

Watremez, L., Prada, M., Minshull, T., O'Reilly, B., Chen, C., Reston, T., et al. (2016). Deep structure of the Porcupine Basin from wide-angle seismic data. In M. Bowman, & B. Levell (Eds.), *Petroleum geology of NW Europe: 50 Years of learning—Proceedings of the 8th Petroleum Geology Conference*. *Geological Society of London*, 199–209. https://doi.org/10.1144/PGC8.26

Wessel, P., & Smith, W. H. F. (1998). New improved version of the generic mapping tools released. *Eos, Transactions American Geophysical Union*, *79*(47), 579. https://doi.org/10.1029/98EO00426

White, R. S., Mckenzie, D., & Onions, R. K. (1992). Oceanic crustal thickness from seismic measurements and rare-earth element inversions. *Journal of Geophysical Research*, *97*(B13), 19,683–19,715. https://doi.org/10.1029/92JB01749

White, R. S., Smith, L. K., Roberts, A. W., Christie, P. A. F., Kusznir, N. J., & iSIMM Team (2008). Lower-crustal intrusion on the North Atlantic continental margin. *Nature*, *452*(7186), 460–464. https://doi.org/10.1038/nature06687

Whitmarsh, R. B., & Miles, P. R. (1995). Models of the development of the West Iberia rifted continental margin at 40° 30′ N deduced from surface and deep-tow magnetic anomalies. *Journal of Geophysical Research*, *100*(B3), 3789–3806. https://doi.org/10.1029/94JB02877

Zelt, C., & Forsyth, D. (1994). Modeling wide-angle seismic data for crustal structure: Southeastern Grenville Province. *Journal of Geophysical Research*, *99*(B6), 11,687–11,704. https://doi.org/10.1029/93JB02764

Zelt, C. A. (1998). Lateral velocity resolution from three-dimensional seismic refraction data. *Geophysical Journal International*, *135*(3), 1101–1112. https://doi.org/10.1046/j.1365-246X.1998.00695.x

Zelt, C. A., & Smith, R. B. (1992). Seismic traveltime inversion for 2-D crustal velocity structure. *Geophysical Journal International*, *108*(1), 16–34. https://doi.org/10.1111/j.1365-246X.1992.tb00836.x